Additive Manufacturing 32 (2020) 101011

Contents lists available at ScienceDirect

Additive Manufacturing

journal homepage: www.elsevier.com/locate/addma

Full Length Article

Selective laser melting of 304L stainless steel: Role of volumetric energy density on the microstructure, texture and mechanical properties

Milad Ghayoor[a,b], Kijoon Lee[a,b], Yujuan He[c], Chih-hung Chang[c], Brian K. Paul[a,b], Somayeh Pasebani[a,b,*]

[a] School of Mechanical, Industrial and Manufacturing Engineering, Oregon State University, Corvallis, OR, 97330, United States
[b] Advanced Technology and Manufacturing Institute (ATAMI), Corvallis, OR 97330, United States
[c] School of Chemical, Biological and Environmental Engineering, Oregon State University, Corvallis, OR, 97330, United States

ARTICLE INFO

Keywords:
304L stainless steel
Additive manufacturing
Selective laser melting
Volumetric energy density
Texture
Microstructure

ABSTRACT

The role of volumetric energy density on the microstructural evolution, texture and mechanical properties of 304L stainless steel parts additively manufactured via selective laser melting process is investigated. 304L is chosen because it is a potential candidate to be used as a matrix in a metal matrix composite with nanoparticles dispersion for energy and high temperature applications. The highest relative density of 99 % ± 0.5 was achieved using a volumetric energy density of 1400 J/mm^3. Both XRD analysis and Scheil simulation revealed the presence of a small trace of the delta ferrite phase, due to rapid solidification within the austenitic matrix of 304L. A fine cellular substructure ranged between 0.4–1.8 μm, was detected across different energy density values. At the highest energy density value, a strong texture in the direction of [100] was identified. At lower energy density values, multicomponent texture was found due to high nucleation rate and the existing defects. Yield strength, ultimate tensile strength, and microhardness of samples with a relative density of 99 % were measured to be 540 ± 15 MPa, 660 ± 20 MPa and 254 ± 7 HV, respectively and higher than mechanical properties of conventionally manufactured 304L stainless steel. Heat treatment of the laser melted 304L at 1200 °C for 2 h, resulted in the nucleation of recrystallized equiaxed grains followed by a decrease in microhardness value from 233 ± 3 HV to 208 ± 8 HV due to disappearance of cellular substructure.

1. Introduction

Metal additive manufacturing (MAM), also known as metal 3D printing, can produce parts with complex geometry and high strength directly from computer-aided design (CAD). Furthermore, the design and manufacturing of the final component can be done in less time and steps in the MAM process compared to conventional manufacturing [1]. The selective laser melting (SLM) process is based on spreading a layer of metal powder onto a platform and laser melting of a predefined slice pattern from the CAD file to the layer below it. This procedure continues layer by layer until the desired component is completely manufactured. The SLM process provides higher resolution, better dimensional accuracy, and greater material flexibility compared with other MAM processes [2,3].

Microstructural characterization and mechanical properties of alloys manufactured via SLM including Ni-based superalloys [4,5], titanium alloys [6,7], aluminum alloys [8], precipitation hardening steels [9–11], ferritic-martensitic steels [12] and austenitic stainless steel (SS) with focus on 316L [13,14] are investigated. For example, Li *et al.* [15] compared the densification of SLM manufactured 316L from water and gas atomized powder and reported less balling effect and higher density of parts made from gas atomized powder due to lower oxygen content and better wettability in the gas atomized powder.

To date, several publications have correlated the effect of printing parameters such as laser power, scan speed, layer thickness and hatch spacing with densification behavior, microstructure and mechanical properties of SLM 316L [13,16,17]. Liverani *et al.* [13] designed a window for process parameters of SLM 316L that could achieve relative densities greater than 98 %. According to Liverani *et al.* [13], laser power significantly influenced relative density whereas building orientation and hatch spacing did not. The highest yield strength (YS of 520 MPa) and ultimate tensile strength (UTS of 650 MPa) was attributed to the sample with a relative density of ≈100 % at the laser energy density of 153.1 J/mm^3. Tucho *et al.* [18] investigated the role of energy density on the porosity, hardness and microstructural evolutions of SLM 316L. According to Tucho *et al.* [18], hardness is directly related to

* Corresponding author at: School of Mechanical, Industrial and Manufacturing Engineering, Oregon State University, Corvallis, OR, 97330, United States.
E-mail address: somayeh.pasebani@oregonstate.edu (S. Pasebani).

https://doi.org/10.1016/j.addma.2019.101011
Received 1 May 2019; Received in revised form 17 October 2019; Accepted 20 December 2019
Available online 27 December 2019
2214-8604/

the density of the SLM manufactured part within the energy density range of 50 − 125 J/mm^3.

304L austenitic SS have excellent corrosion resistance, high oxidation resistance, and superior mechanical properties at room temperature due to high Cr content. Applications of 304L vary from nuclear reactor components to chemical processing equipment, and oil industries [19,20]. Furthermore, 304L is a promising candidate to be used as a matrix in oxide dispersion strengthened (ODS) steel where oxide nanoparticles are dispersed within 304L matrix. However, few studies have been published on the additive manufacturing of 304L SS parts. Most of current literature [21–24] are focused on the role of processing parameters on mechanical properties. Whereas, the effect of processing parameters on microstructural evolutions and texture during SLM of 304L is missing in the literature.

Guan et al. [21] investigated the effect of overlap rate, layer thickness, building orientation and hatching angle on tensile properties of SLM 304L SS. According to Guan et al. [21], tensile properties are independent of layer thickness (in the range of 20 − 40 μm) and overlap rate (in the range of 0–50 %). Nevertheless, the microstructure of SLM 304L has not been discussed in their work. Furthermore, Elghany et al. [22] studied the effect of layer thickness and scanning speed on density, surface roughness and tensile properties of SLM 304L; reporting the maximum yield and ultimate tensile strength of 182 and 393 MPa, respectively, corresponding to the layer thickness of 30 μm and scan speed of 70 mm/s. Yu et al. [23] explored the main cause of mechanical anisotropy in SLM 304 SS by analyzing the microstructure and texture of samples; reporting the higher columnar length-width ratio of grains, yielded to the higher mechanical anisotropy. Wang et al. [24] studied the impact of process parameters in a directed energy deposition (DED) process on mechanical properties of thin walls manufactured using 304L SS. The highest YS and UTS were reported to be 337 ± 29 MPa and 609 ± 18 MPa, respectively. Therefore, there is a critical gap in current literature on a comprehensive understanding of the microstructural, phase and texture evolution of 304L SS during SLM.

The SLM process exhibits a complex metallurgical mechanism depending on the processing parameters, material characteristics and chemical compositions. The adoption of different combination of these parameters greatly affect the part formation quality and lead to variations of microstructure and mechanical properties [25]. Hann et al. [26] demonstrated that the welding data from different experiments with various materials and parameters could all be represented on one curve under the assumption that the melt pool depth (d) divided by the beam size (σ) is a function of the deposited energy density (ΔH) to the enthalpy at melting point (h_s). According to this model, the ratio $\Delta H/h_s$ is defined as:

$$\frac{\Delta H}{h_s} = \frac{AP}{\pi h_s \sqrt{Dv\sigma^3}} \quad (1)$$

where A is absorptivity, P is laser power, D is thermal diffusivity of the molten material and v is scan speed. King et al. [27] have validated similar scaling for laser bed fusion process, showing that the transition from conduction mode to keyhole mode of laser melting occurs around $\Delta H/hs \approx (30 \pm 4)$. They concluded that this threshold for keyhole mode of melting could help to identify the optimum process parameters. The proposed model mostly was adopted by researchers in single-track experiments to correlate energy density to the shape and size of the melt pool, melting mode (conduction or keyhole), spattering and in-situ monitoring of laser-powder interaction [28,29]. However, most of the previously mentioned studies [13,16–18] have often presented their results on SLM manufactured solid part using an approach based on the volumetric energy density (VED) which is expressed as:

$$E = \frac{P}{v \times h \times t} \quad (2)$$

where h is hatch spacing and t is layer thickness. In their studies, the VED was used as a metric for each printing parameters in order to correlate the final SLM manufactured part density, surface finish, microstructure and mechanical properties [13,16–18]. For example, Kurzynowski et al. [17] investigated the influence of laser power and scanning strategy, using VED, on microstructure and texture of manufactured SLM 316L parts, finding that the VED strongly affected the microstructure and the amount of ferrite phase. It is noted that the VED can be utilized in combining the effects of laser power, scan speed and layer thickness to calculate the energy delivered per unit volume of powder bed and serves as a guideline for parameter selection to get the highest density. According to Bertoli [30,31] the VED is limited to accurately describe the mode of melting which needs information on the complex science of melt pool [30,31].

Thus, the novelty of this work is to determine phase evolution of 304L SS during the SLM process and identify the effect of VED on solidification and densification behavior, microstructural evolutions and mechanical properties of SLM 304L samples. Furthermore, this study investigates the role of VED on imposing a texture in 304L samples processed by various VED values applied in SLM process. Additionally, microstructure, phase and mechanical properties of SLM 304L sample after annealing are investigated.

2. Experimental

2.1. Powder feedstock

Sandvik Osprey gas-atomized AISI 304L austenitic SS powder (< 45 μm), with the chemical composition given in Table 1, was used as the feedstock. A particle size distribution analysis was done using a Malvern Analytical particle analyzer (Mastersizer 3000). Apparent density (AD) and tap density (TD) were measured according to ASTM B212-17 (Hall Flowmeter Funnel) and ASTM B527-15, respectively. The flowability of the powder was measured using the Hausner ratio (AD/TD).

2.2. SLM process

An ORLAS Creator Metal 3D printer (OR Laser/ Coherent) with a continuous wave fiber laser of 250 W Yb:YAG and a wavelength of 1067 nm was used for the SLM process. The ORLAS Creator utilizes a rotational coater mechanism and beam expander which enables the focal spot size (1/e^2, Gaussian beam) of the laser to be adjusted between 40–180 μm.

Fig. 1(a) shows the build chamber of the OR Creator SLM machine. Three sets of twelve cylinders, randomly orientated on the build platform, with a dimension of R4 × 8 mm, as shown in Fig. 1(b), were additively manufactured on the 316 SS substrate with following parameters; laser power 105 W, scan speed 50 − 600 mm/s with an increment of 50, spot size 50 μm, hatch spacing 50 μm, layer thickness 30 μm and scan rotation angle of 105°. The scan rotation angle of 105° showed the highest yield strength compare to other scan rotations according to Guan *et al.* [21]. According to the provided formula of energy density (Eq. 2), the VED for the adopted scan speeds of 50–600 mm/s in this experiment were calculated to be in the range of 117–1400 J/mm^3. The atmosphere inside SLM chamber was commercially pure nitrogen. The oxygen level of the sealed SLM chamber was consistently kept < 100 ppm by continuously purging pure nitrogen.

2.3. Microstructure characterization and mechanical testing

Sample density was measured according to the Archimedes method.

Table 1
Chemical composition of 304L stainless steel powder.

Element	Cr	Ni	Fe	C	Si	Mn	P	S	N
wt.%	18.853	10.060	Bal	0.017	0.720	1.3	0.012	0.005	0.083

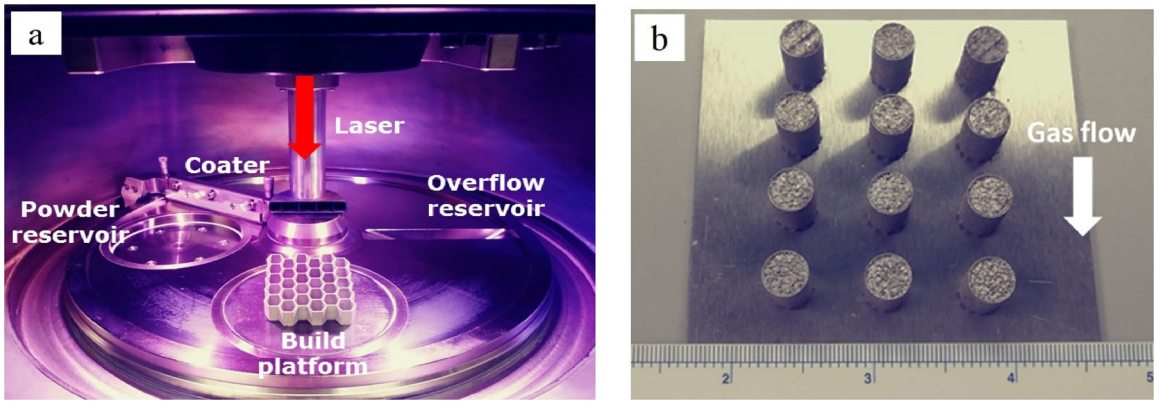

Fig. 1. (a) OR Creator's build chamber and (b) SLM 304L cylinders on the build plate.

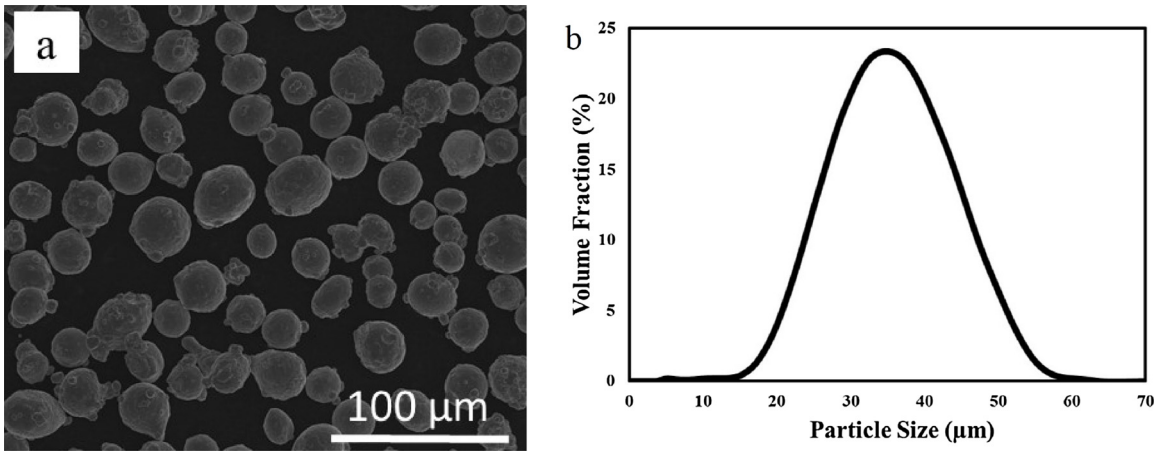

Fig. 2. (a) SEM micrograph showing morphology and (b) particle size distribution histogram of 304L powder.

Phase identification for both 304L SS powder and SLM samples was done using X-ray diffraction (XRD) analysis (Bruker AXS D8 Discover), operating with Cu Kα radiation at 40 kV, with a step size of 0.05° and 2θ, ranged from 20-100°. Microstructural characterization of samples was done using optical microscopy (Zeiss, Axiotron) and scanning electron microscopy (SEM) on both perpendicular and parallel to build direction. An FEI Quanta 3D SEM equipped with electron dispersive X-ray spectroscopy (EDS) was utilized. Sample preparation was accomplished according to standard metallographic procedures. Polished samples were electroetched for 15 s at an applied DC voltage of 15 V using an electrolyte solution of 10 wt.% oxalic acid.

Electron backscattered diffraction (EBSD) was performed on vibratory polished samples with 50 nm diamond suspension for 8 h. The EBSD data collection was conducted by using an Orientation Imaging Microscopy (OIM) Data Collection 7.2 software in FEI Quanta 3D operating at 15 kV accelerating voltage, 1.7 nA beam current and a step size of 50 nm. The collected data were processed using OIM Analyses 7.2 software. Transmission electron microscopy (TEM) analysis of SLM samples was done using a TEM/STEM model FEI TITAN 80–200 equipped with ChemiSTEM technology. The TEM samples were prepared, first by thinning down mechanically to a thickness of about 50–100 µm. Then, 3-mm diameter disks were punched out of the thinned disks and were electropolished using a Fischione-110 twin-jet electropolisher operated at a potential of 15 V and temperature of −30 °C. The solution of methanol (75 vol.%) and nitric acid (25 vol.%) were used as an electrolyte.

Microhardness of the SLM 304L samples was measured using a microhardness tester (Leco, LM-248AT) at a load of 500 g. The average value from 10 random indentations is reported in the results. Horizontal blocks with a dimension of 94 × 10 × 8 (L × W × T) mm were manufactured using different SLM parameters. Three tensile test coupons with a thickness of 2 mm were cut using a wire electrical discharge machining (EDM) from each block. The tensile specimens were machined according to the sub-size specimen specification of ASTM E8. The average value of three tensile tests is reported in the results. The tensile test was conducted on an Instron 5969 at a strain rate of 10^{-4} s^{-1} and at room temperature.

In order to predict different phases during SLM processing, a Scheil model for non-equilibrium solidification was performed using Thermo-Calc software integrated with a TCFE8 database. The simulation was performed for a step size of 1 °C from the liquid phase up to the remaining liquid fraction reach the 0.1. The SLM 304L sample with VED of 233 J/mm^3 was annealed at 1200 °C for 2 h in a vacuum furnace, and cooled in furnace. The microstructure and phase evolution of the annealed sample was investigated using XRD, SEM, and EBSD as described formerly.

3. Results and discussion

3.1. Characterization of 304L powder feedstock

Morphology of 304L powder, used as feedstock in this study, is shown in Fig. 2(a). Fig. 2(b) shows the normal histogram of particle size distribution obtained from Malvern particle size analyzer.

Gas atomized 304L powder showed spherical particles with some satellites. Particle size distribution analysis, AD, TD and Hausner ratio of 304L powder are listed in Table 2. The average particle size was approximately 33 µm and the majority of particles were < 45 µm. Hausner ratio for 304L powder was 1.31. Hausner ratio greater than 1.25 shows relatively poor flowability [32], mostly due to the tendency

Table 2
Physical properties of 304L SS powder measured in this study.

Particle size distribution (μm)			Apparent density (g/cc)	Tap density (g/cc)	Hausner ratio (AD/TD)
D_{10}	D_{50}	D_{90}	3.59	4.69	1.31
23.4	33.2	43.7			

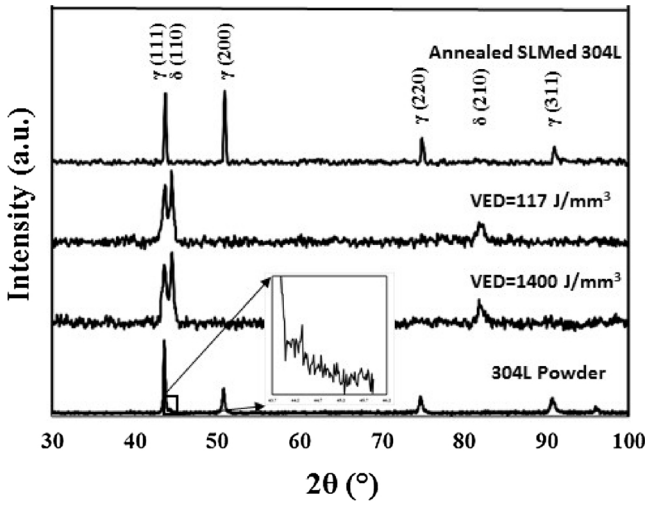

Fig. 3. XRD pattern of 304L powder, SLM 304L with VEDs of 117 and 1400 J/mm^3 and SLM 304L with VED of 233 J/mm^3 annealed at 1200 °C.

of small particles locking bigger particles; increase the interparticle friction; and imped powder movements and flow. However, no agglomeration was formed during spreading of powder into a thin layer in the SLM machine, and the flowability of this powder was acceptable for SLM processing.

Fig. 3 shows the XRD patterns of precursor 304L powder, SLM 304L at VED of 117 and 1400 J/mm^3, and SLM 304L at VED of 233 J/mm^3 followed by annealing at 1200 °C (as will be discussed in Section 3.7).

In 304L feedstock powder, the major phase with the highest peak intensity was identified as austenite (γ), however, a small peak of ferrite (δ) was identified. The Rietveld refinement method [33] showed that the amount of austenite and ferrite in 304L SS powder was 98.5 wt.% and 1.5 wt.%, respectively. A fully austenitic SS is susceptible to hot cracking during welding due to the limited solubility of phosphorus (P) and sulfur (S) in the FCC-austenitic phase. Because P and S are susceptible to segregation at grain boundaries due to the lower melting point than Fe.

Having a small amount of ferrite in 304L, with a higher solubility for P and S, would minimize the harmful effect of P and S [34,35]. This can be accomplished by controlling the ratio of Cr_{eq}/Ni_{eq} ($Cr_{eq} = Cr + Mo + 1.5Si + 0.5Nb$; $Ni_{eq} = Ni + 30C + 0.5\ Mn$) and shifting the mode of solidification from completely austenitic to a mixture of austenite and ferrite. The higher the ratio of Cr_{eq}/Ni_{eq}, the higher the fraction of ferrite will be produced [34].

According to the ratio of Cr_{eq}/Ni_{eq}, the primary solidification behavior of austenitic SS can be divided into four different categories [36]:

1) Austenitic mode: $L \rightarrow L + \gamma \rightarrow \gamma$ $Cr_{eq}/Ni_{eq} < 1.25$
2) Austenitic-ferritic mode: $L \rightarrow L + \gamma \rightarrow L + \delta + \gamma \rightarrow \gamma + \delta \rightarrow \gamma$ $1.25 < Cr_{eq}/Ni_{eq} < 1.48$
3) Ferritic-austenitic mode: $L \rightarrow L + \delta \rightarrow L + \delta + \gamma \rightarrow \gamma + \delta \rightarrow \gamma$ $1.48 < Cr_{eq}/Ni_{eq} < 1.95$
4) Ferritic mode: $L \rightarrow L + \delta \rightarrow \delta \rightarrow \delta + \gamma \rightarrow \gamma$ $Cr_{eq}/Ni_{eq} > 1.95$

For the 304L feedstock powder used in this study, the Cr_{eq}/Ni_{eq} ratio was calculated to be 1.75 ($Cr_{eq}/ Ni_{eq} \cong 19.85/11.25$), which falls into the ferritic-austenitic mode and, thus, not susceptible to hot cracking during the process.

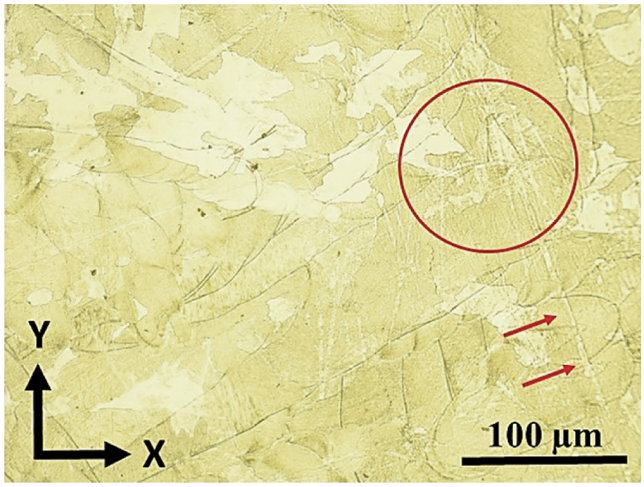

Fig. 4. Optical micrograph of SLM 304L with VED of 375 J/mm^3; circle shows a cluster of needle shape ferrite phase and arrows show large needles attributed to δ-ferrite.

3.2. Characterization of SLM 304L parts

Fig. 3 shows the XRD pattern at the lowest and highest VED values (117 and 1400 J/mm^3). The major peak in SLM parts was attributed to the ferrite phase (110), and a lower intensity of the austenite phase was observed. Therefore, a strong texture of the ferrite phase was expected in SLM 304L SS. Solidification of 304L austenitic SS starts by nucleation of δ-ferrite growing in dendritic morphology. Through further cooling, the solid-state transformation of δ-ferrite to austenite would progress. However, the transformation could not get completed due to the high cooling rate of SLM process and non-equilibrium condition of SLM process. Therefore, δ-ferrite would remain at the cores of the primary and secondary dendrite arms at room temperature. This dual-phase of austenite (γ) and ferrite (δ) were observed in the microstructure of the SLM material as will be shown in Fig. 4. No ferrite (δ) peak was observed after annealing at 1200 °C, and fully austenitic 304L was achieved.

An optical micrograph of SLM 304L sample at VED of 375 J/mm^3 is shown in Fig. 4. A cluster of needle-shaped phase attributed to the presence of remnant dendritic δ-ferrite in austenitic phase due to rapid cooling is marked with a circle. The needle characteristic of δ-ferrite phase could impose a high degree of texture for the ferrite phase.

Scheil equation could predict different phases in the non-equilibrium rapid cooling process such as SLM. Therefore, Thermo-Calc Scheil simulation was performed on the 304L composition used in this study, and the results further confirmed the presence of retained δ-ferrite (BCC_A2) in the 304L austenitic (FCC_A1) matrix as shown in Fig. 5.

3.3. Microstructure of SLM 304L parts

Optical micrographs of SLM 304L parts obtained from different cross-sections (parallel and perpendicular to build direction) are shown in Fig. 6(a–d). In Fig. 6(a), laser path, and rotation angle of 105° between two subsequent layers are annotated in the perpendicular cross-section. The relative density of the sample produced at a VED of 1400 J/mm^3 was 99 ± 0.5 %. The relative density for the sample that was produced at the lowest VED of 117 J/mm^3 was 94 ± 1.7 %.

Fig. 6(a) and (c) present optical micrographs of perpendicular and parallel cross-sections of the sample with the highest VED of 1400 J/

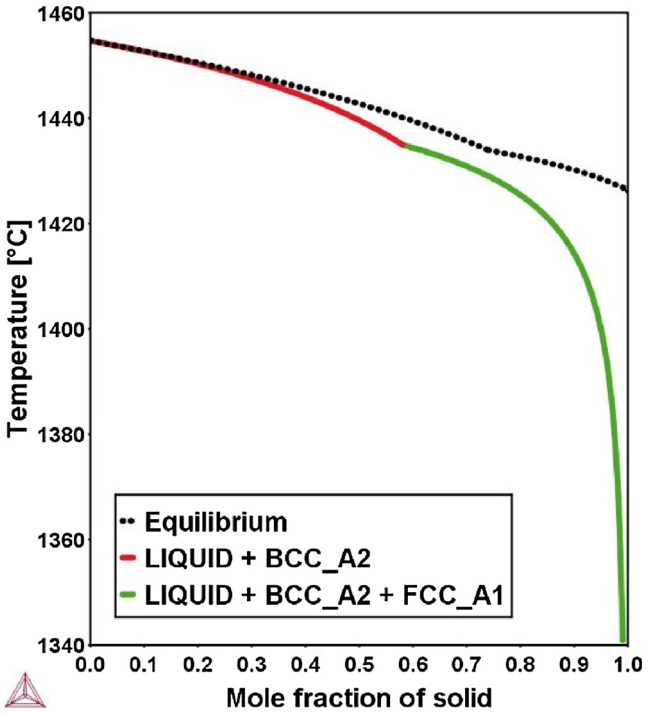

Fig. 5. Scheil simulation of rapid cooling of 304L SS, presenting the formation of δ-ferrite (BCC_A2) and austenitic (FCC_A1).

mm^3. Fig. 6(b) and (d) show micrographs of perpendicular and parallel cross-sections of the sample with the lowest VED of 117 J/mm^3. Very few small pores were observed at a cross-section perpendicular to the build direction as marked by a circle in Fig. 6(a). There was no evidence of large porosity or cracks between the layers in Fig. 6(c). Furthermore, small porosities were located at the center of the melt pool where the temperature is the highest during SLM process. According to Table 1, the 304L powder contained 0.083 wt.% of nitrogen, which was due to gas atomization process. Therefore, small and spherical porosity shown with small dashed circles could be attributed to gas entrapment of powder feedstock and absorption of nitrogen gas during solidification in the SLM process.

Absence of large porosity and the balling effect in Fig. 6(a) and (c) is due to low oxygen content (100 ppm) and a high VED of 1400 J/mm^3. In order to relatively compare the melt pool sizes of manufactured parts using different VEDs, the top layer melt pool characterization method was adopted to measure the depth of melt pool boundaries at the last printed layer on the cross-section parallel to build direction (xz) [37]. The schematic in Fig. 7 shows the characterization metric of d_p/t_L, the ratio of full melt pool depth to nominal layer thickness, and d_0/t_L, the ratio of melt pool overlap depth to nominal layer thickness. The measured data for different VEDs are provided in Table 3. The purpose of this measurement was to relatively compare the size of melt pools as a result of using different VEDs and subsequently to show the role of melt pool size (melt volume) on densification of SLM manufactured parts.

The d_p/t_L and d_0/t_L of the melt pool boundaries for VED of 1400 J/mm^3 were 5.04 and 3.91, respectively. For VED of 117 J/mm^3, the d_p/t_L and d_0/t_L were measured to be 1.46 and 1.09, respectively. The higher ratio of d_p/t_L and d_0/t_L in higher VEDs suggests that the volume of melt pool is proportional to the VEDs and thus, inversely proportional to the

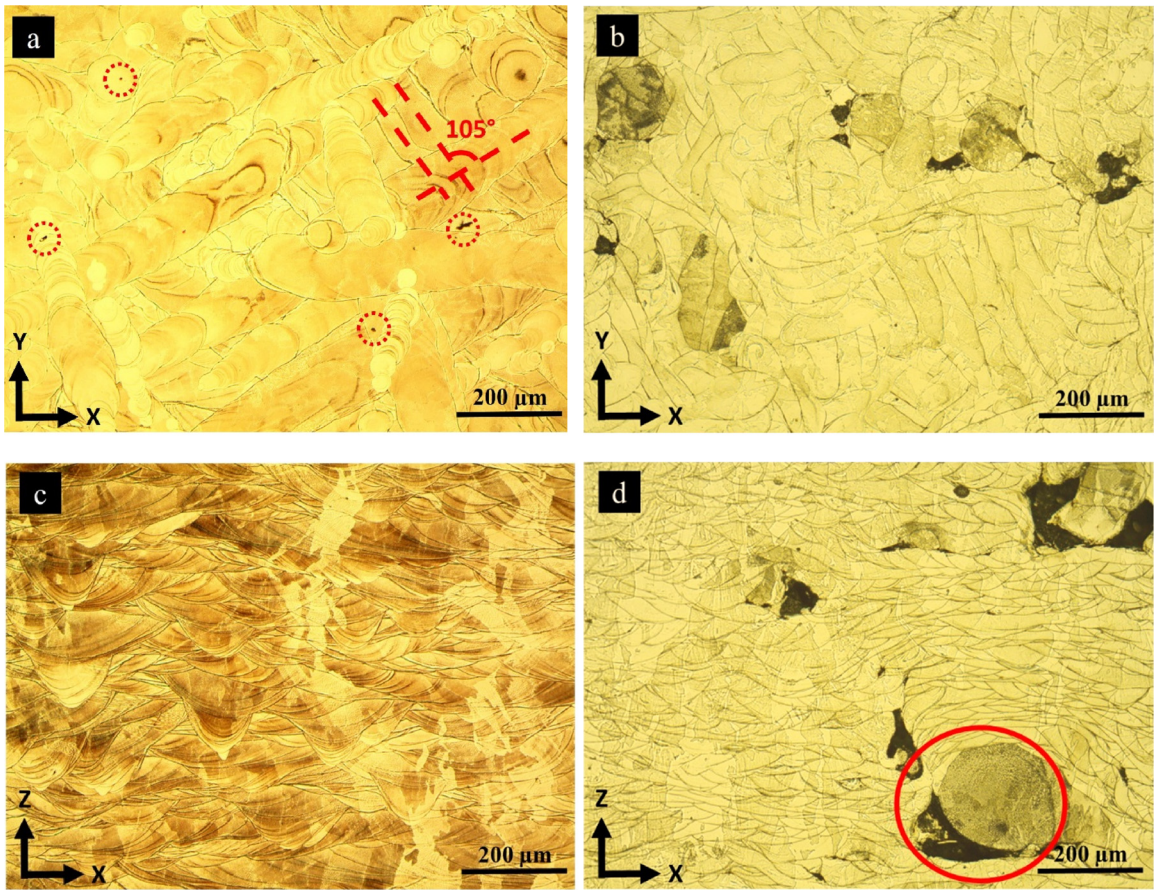

Fig. 6. Optical micrograph from cross-section, perpendicular to build direction, at VED of (a) 1400 J/mm^3 and (b) 117 J/mm^3 and from cross-section, parallel to build direction, at VED of (c) 1400 J/mm^3 and (d) 117 J/mm^3.

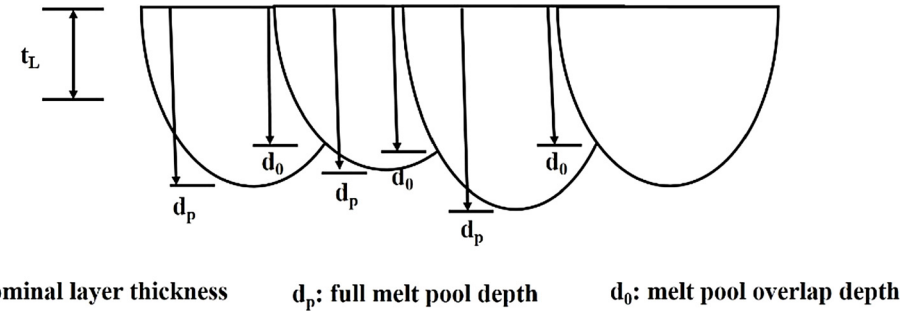

Fig. 7. Schematics of top layer melt pool measurements on X-Z cross-section.

Table 3
The d_p/t_L and d_0/t_L of melt pool boundaries measured at different VEDs.

VED (J/mm^3)	d_p/t_L	d_0/t_L
1400	5.04 ± 0.22	3.91 ± 0.21
700	3.66 ± 0.39	1.97 ± 0.31
350	1.83 ± 0.31	1.22 ± 0.13
117	1.46 ± 0.19	1.09 ± 0.12

scan speed (Eq. 2). The higher VED value, the greater the amount of heat is that can melt and fill porosity to enhance densification.

Another explanation for the improved densification at the highest VED of 1400 J/mm^3 can be explained by the dynamic viscosity (μ) of the molten pool as defined by the following equation: [38]:

$$\mu = \frac{16}{15}\left(\sqrt{\frac{m}{kT}}\gamma\right) \tag{3}$$

where m is the atomic mass, k is the Boltzmann constant, T is the absolute temperature, and γ is the liquid surface tension. According to Eq. 3, μ decreases at high energy density, as a result of higher T and lower γ_{sl}. When the melt viscosity decreases, it can spread more easily onto the previously solidified layer to prevent the balling effect and fill porosity. Furthermore, a sharp thermal gradient/composition gradient across the surface induced by high energy density leads to surface tension gradients known as Marangoni convection flow.

Marangoni convection is a driving force for fully spreading the melt onto the previous layer and enhancing densification at higher VEDs [39]. As a result, the combined effects of lower viscosity and Marangoni convection flow and larger volume of melt are the key factors leading to enhanced densification behavior. Non-uniformly distributed irregular-shaped porosities were observed in the sample with the lowest VED of 117 J/mm^3, as shown in Fig. 6(b) and (d). Elongated voids were present at the melt pool boundaries due to lack of adhesion between the adjacent layers. The formation of elongated voids is likely due to insufficient VED (117 J/mm^3) for melting the previously deposited layer.

A particle with a diameter of 200 μm which is significantly larger than the initial particle size is shown in Fig. 6(d). Formation of such a large particle could be likely due to three possible phenomena; (1) high scan speed would cause turbulent splashes inside the melt pool due to large shear forces and these splashes would be displaced to the outside of laser path and be solidified as a large particle; (2) high viscosity of the melt could lead to balling effect forming a spherical shape [13]; and (3) the high intensity of laser beam could cause metal vaporization and lead to recoil pressure and spatter ejection from the surface [40]. These large particles disturb the spreading of the powder in the subsequent layers by blocking the powder. Furthermore, these particles could not be melted at the next layer and were remained unmelted due to combined effects of high scanning speed and low VED. Absence of sufficient volume of the powder on the opposite side of this large particle, and lower viscosity of melt did not provide sufficient amount of melt for filling the voids. Eventually, the void became larger with adding layers and reduced the relative density of the part.

A lighter contrast of elongated grains caused by columnar grain growth on xz plane is shown in Fig. 6(c). The formation of elongated grains could be explained because of coherency in chemistry and crystallography between the melted powder and the previously solidified layer. Thus, there was no barrier against nucleation of new grains [41] which could grew at the same crystal orientation of the previous layer until this similarity in chemistry or crystallography was altered either due to the formation of defects such as voids, porosity or balling effect. At high VED, because of the slow movement of heat source, there could be a profound direction of thermal gradient and sufficient time for the melt to solidify in the preferred orientation. This is likely why the preferred orientation and larger columnar grains were formed at high VED of 1400 J/mm^3 as shown in Fig. 6(c).

The higher number of defects were observed at high scan speed and low VED as shown in Fig. 6(d). Defects such as voids could locally change the direction of heat flux in such a way that epitaxial grain growth (which follows the dissipation direction) could be different from the build direction. The combined effect of alternating direction of heat flux and Marangoni convection inside the melt pool likely led to more collision of grains, resulting in finer grain size.

SEM micrographs of the SLM 304L sample at VEDs of 1400, 350, 175 and 117 J/mm^3 are shown in Fig. 8(a)–(d), respectively. A hexagon pattern was shaped on the surface of the electroetched sample as presented in Fig. 8(a). The hexagon pattern is a cluster of cells or subgrains that were formed during rapid solidification. The brighter contrast of cell walls (or subgrain boundaries) could be attributed to the segregation of heavier elements such as Cr and presumably high density of dislocations [18].

Fig. 8(a)–(d) demonstrated that different VEDs led to different sizes of cellular substructure. Furthermore, by decreasing VED from 1400 to 117 J/mm^3, the size of each cell was reduced subsequently. During SLM process the temperature gradient in liquid (G_L), growth rate (R), and solidification undercooling (ΔT) varies from center to the edge of the melt pool. The effect of the solute and thermal gradient on the substructure is formulated by the equation below [41]:

$$\frac{G_L}{R} < \frac{\Delta T}{D_L} \text{ forsteady- stateplanargrowth}$$

$$\frac{G_L}{R} > \frac{\Delta T}{D_L} \text{forcellularandcolumnargrowth}$$

where D_L is the diffusion coefficient of liquid. Here, the G_L/R ratio governs the solidification microstructure, and the cooling rate ($G_L \times R$) determines the size of the substructure. The higher cooling rate would result in the finer substructure [41].

The planar interface is randomly orientated because the growth is controlled by the heat flow, and, the direction of growth is perpendicular to the solidification front. Cellular growth in terms of growth direction is very similar to planar growth and is controlled by heat flow and crystallographic orientation. The main characteristic of cellular growth is uniformly spaced cells or hexagons, growing parallel to each other as shown in Fig. 8(a)–(d). Dendritic growth is completely

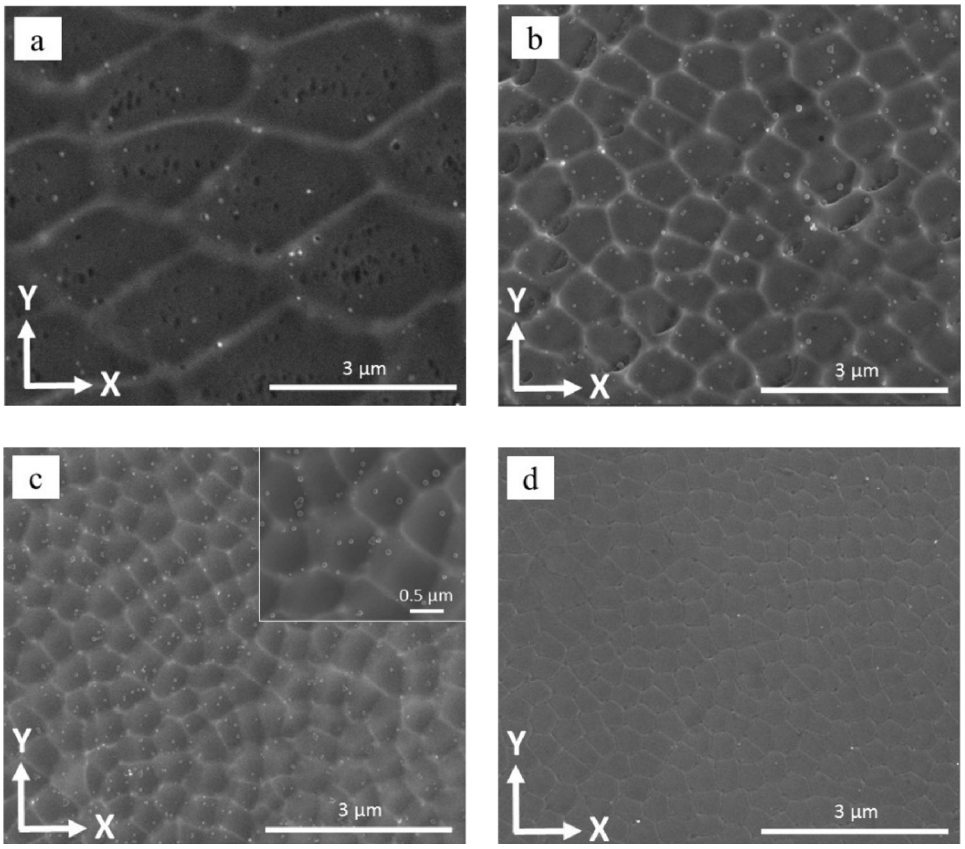

Fig. 8. SEM micrographs of SLM 304L, perpendicular to build direction, with different VEDs: (a) 1400 J/mm^3, (b) 350 J/mm^3, (c) 175 J/mm^3 and (d) 117 J/mm^3.

different from planar and cellular growth. In dendritic growth, the crystallographic orientation governs the direction of growth. Dendritic growth occurs in a specific direction, known as easy growth direction where growth and solidification rates are the fastest [42].

The formation of very fine nanoparticles was evident in the inset shown in Fig. 8(c) from SLM 304L at VED of 175 J/mm^3. These nanoparticles were formed and distributed across the surface in all of the samples. The distribution of nanoparticles was not uniform and varied in different regions of the sample. Further investigation was done by TEM to characterize these nanoparticles, and results are presented in Section 3.4.

In order to quantitatively compare the size of cells at each VED (117 − 1400 J/mm^3), the average cell size was measured according to Ma *et al.* [43] procedure. The measurement was done on 20 random regions on the cross-section perpendicular to building direction. The average values are plotted in Fig. 9.

In Fig. 9, the cooling rate was calculated from primary cellular arm spacing according to the following equation [36]:

$$\lambda = 80\dot{T}^{-0.33} \quad (4)$$

where $\dot{T}$ is the cooling rate, and λ is the primary cellular arm spacing. Fig. 9 shows an increase in cell size and a reduction in the cooling rate at higher VEDs. The highest and lowest cooling rates were 10^7 K/s and 10^5 K/s associated with VED of 117 J/mm^3 and 1400 J/mm^3, respectively. Due to the high cooling rate (10^5-10^7 K/s), there was not sufficient time for the growth of branches originating from the primary arms. Thus, the formation of dendritic microstructure was unlikely, as indicated in Fig. 8(a)–(d). At lower VEDs, cooling rates were significantly increased especially at VEDs < 400 J/mm^3. In contrast, at higher VEDs, the cooling rate was slightly decreased.

In the sample with the highest VED (1400 J/mm^3), the cells were approximately uniform in size and orientation across different regions of the sample. The hexagon pattern and elongated cell walls were the dominant patterns in the cross-sections perpendicular and parallel to build direction, respectively. However, at lower VEDs (117 − 200 J/mm^3), a predominant pattern in different cross-sections was absent. In other words, both hexagon pattern and elongated cell walls could be found very close to each other in perpendicular and parallel cross-sections, especially in the vicinity of defects such as porosity.

Because porosity and voids act as internal heat sink inside the SLM sample altering the cooling rate and subsequently cell size and orientation of cellular substructure. This observation was consistent with directionality in the growth of grains in the optical micrograph shown in Fig. 6(d). It can be implied that the directionality in substructure would cause the grains or macrostructure to get orientated in the same direction of the cellular substructure and form a hierarchical structure that will be discussed in Section 3.5.

3.4. TEM characterization of SLM 304L parts

The SLM 304L contains nanoparticles that were precipitated upon rapid cooling within the matrix as formerly shown in Fig. 8(c). These nanoparticles are shown at higher magnification in the STEM micrograph depicted in Fig. 10(a). The diameter of these spherical particles varied from 20 to 80 nm as shown by arrows in Fig. 10(a). The distribution of these nanoparticles was not found to be uniform throughout the entire sample. High dislocation density and cellular structure were evident features in Fig. 10(a).

In addition to nanoparticles, parallel and oblique band features were evident in the STEM micrograph shown in Fig. 10(b). Tucho et al. [18] identified these bands as twining structures formed due to plastic deformation of the matrix as a result of high thermal stress induced by rapid heating and cooling during the SLM process. The formation of nanotwins during the tensile test was formerly reported in the SLM 316 SS [44]. However, thermally-induced nanotwins were not formerly reported during SLM of 304L SS. Additional discussion is provided in

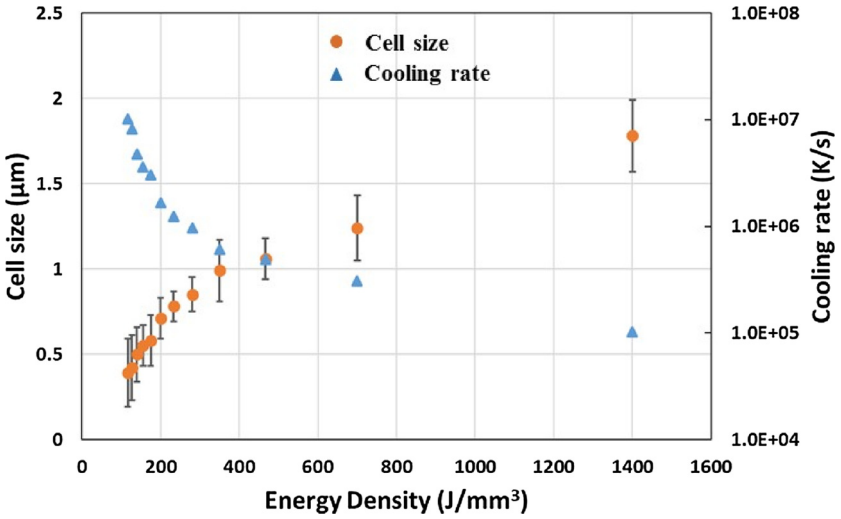

Fig. 9. The effect of VED on cell size and cooling rate in SLM of 304L SS (data points are plotted for VED of 117 − 1400 J/mm^3).

Section 3.6.

The EDS elemental map is obtained from precipitation displayed in Fig. 10(a), and is presented in Fig. 11. The EDS map revealed that these particles mainly consisted of Si, Mn, and O. Table 4 compares the point analysis obtained from the matrix of SLM 304L and obtained from the nanoparticles. According to Table 4, Cr and Ni contents of nanoparticles were lower compared to the 304L matrix. However, the amount of Si, Mn, and O were higher in nanoparticles compared to 304L matrix.

Based on the Ellingham diagram for the oxidation of individual elements [45] as listed in Table 5, the Gibbs free energy for the formation of SiO_2 and MnO are the lowest among the other elements present in 304L. For example, the partial pressure of oxygen at melting temperature of 304L (1400 °C) is 7.1×10^{-20} atm for Si, 1.9×10^{-6} atm for Ni and 3.15×10^{-15} atm for Cr. Thus, the formation of Si-Mn-O-enriched nanoparticles is likely due to the reaction of Si and Mn with any residual oxygen available in the nitrogen-filled SLM chamber.

The required amount of oxygen for reacting with Si and Mn was mainly attributed to the residual of oxygen inside the SLM chamber. Saeidi et al. [14] identified nanoparticles with a diameter of 150 nm that were non-uniformly distributed throughout SLM 316 matrix. However, nanoparticles in this study had diameter of 20–80 nm. The formation of finer nanoparticles in this study is attributed to the lesser available oxygen in SLM chamber (< 0.01 %). The residual oxygen in Saeidi et al. [14] study was < 0.1 %. In another study by Sun *et al.* [16], on SLM 316L, the size of nanoparticles was reported in the range of 100–200 nm, while the oxygen content was at 0.16 %. Comparing the size of nanoparticles and oxygen content in this study with the above-mentioned studies [14,16] implies that the size of nanoparticles is reduced at lower amount of residual oxygen inside SLM chamber. Thus, by understanding the role of oxygen content and minimizing its amount, finer nanoparticles were achieved.

3.5. EBSD result and texture analysis

EBSD maps were performed on a cross-section perpendicular to the build direction of various VEDs to analyze the grain size, morphology, and grain orientation. Table 6 presents the average grain size at VEDs of 1400, 700, 350 and 117 J/mm^3. The grain size was reduced from 10.3 µm to 5.5 µm with decreasing VED from 1400 to 117 J/mm^3. The lower VEDs lead to a higher cooling rate, higher undercooling and consequently smaller critical radius (r*) and thus, lower nucleation energy barrier (ΔG*) [41]. Therefore, using lower VEDs could result in a higher rate of nucleation and eventually the formation of more grains and finer size. Formation of finer grain size by decreasing VED is consistent with the formation of smaller cells formerly discussed in Section 3.3 confirming that SLM parts could show hierarchical structure.

Fig. 12(a)–(d) show the Inverse Pole Figure (IPF) maps and corresponding Pole Figures from cross-section perpendicular to the build direction at VEDs of 1400, 700, 350 and 117 J/mm^3, respectively. Fig. 12(a) revealed the strong texture of {101} at the highest VED of 1400 J/mm^3 due to the high intensity of {101} pole figure when the standard (001) stereographic projection was superimposed to the {101} pole figures. So, the texture of SLM 304L at the highest VED can be described as (101) [100]. The < 100 > direction in cubic systems is the preferred growth direction (easy growth) and this direction is consistent with the texture of the SLM 304L part at the highest VED of 1400 J/mm^3. At the highest VED of 1400 J/mm^3, the laser generates a large volume of melt which could potentially eliminate any heterogeneity or anisotropy in the microstructure of previously solidified layer and provide sufficient time for grains to orient to the opposite direction of

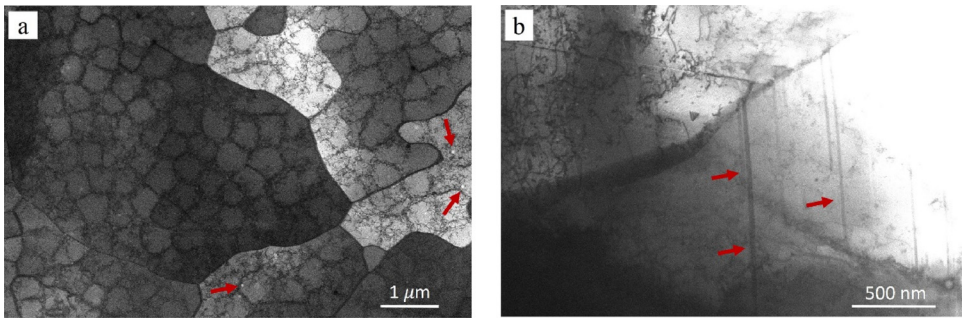

Fig. 10. STEM micrograph of SLM 304L at VED = 350 J/mm^3, parallel to the build direction cross-section, (a) presenting cellular substructure and nanoparticles (pointed by arrows) and (b) showing nanotwins (pointed by arrows).

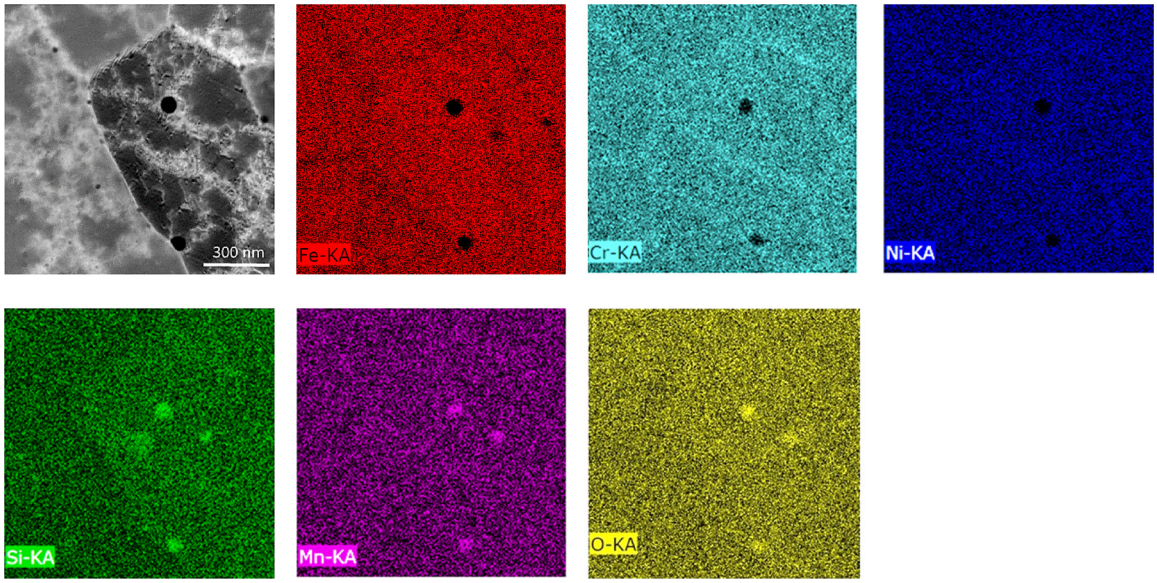

Fig. 11. HAADF STEM image with corresponding EDS elemental map obtained from nanoparticles within the SLM 304L matrix at VED = 350 J/mm^3.

Table 4
Chemical analysis by EDS point analysis performed on both matrix of 304L and nanoparticles in SLM 304L.

Elements	Fe	Cr	Ni	Mn	Si	O	Total
Matrix (wt.%)	67.10	18.18	10.05	1.80	1.33	1.54	100
Nanoparticles (wt.%)	54.01	16.49	8.19	8.49	4.94	7.88	100

Table 5
The equilibrium oxygen partial pressure for the formation of various oxide compounds at 1400 °C [45].

Element	Stoichiometric Composition	P_{O2} (atm)
Fe	Fe_3O_4	7.29×10^{-10}
	Fe_2O_3	6.02×10^{-9}
Cr	Cr_2O_3	3.15×10^{-15}
Ni	NiO	1.90×10^{-6}
Si	SiO_2	7.10×10^{-20}
Mn	MnO	8.10×10^{-18}

Table 6
Grain size measurement for different VEDs by EBSD.

VED (J/mm^3)	1400	700	350	117
Average grain size (μm)	10.3	7.9	6.1	5.5

heat flux, resulting in a high degree of texture in the < 001 > direction.

The multicomponent cubic texture was observed in SLM 304L when the VED decreased from 1400 J/mm^3 to 700, 350 and 117 J/mm^3. Thus, lack of a preferred orientation was observed in different directions of < 100 > , < 110 > and < 111 > . Relatively weak texture in samples manufactured at lower VEDs could be explained by the higher cooling rate causing a higher number density of nuclei and finer grains in random directions. However, the preferred direction of grain growth was altered, and texture became deviated from the direction of the heat-dissipating at lower VED due to presence of porosity and lack of fusion. Yu et al. [23] reported a very weak texture in SLM 304 at VED of 125 J/mm^3. A study by Niendorf *et al.* [46] shows the formation of elongated grains parallel to the build direction, and texture in the direction of < 001 > at a high intensity of 1000 W. However, the presence of the preferred texture at much lower laser power (105 W) is reported in this study. While more investigation is required, our preliminary results on the texture of SLM 304L demonstrates the potential of manufacturing parts with tailored texture and properties via manipulating the SLM parameters and direction of the build.

3.6. Mechanical properties

Relative densities and microhardness values as a function of VED are plotted in Fig. 13 (a) and (b), respectively, for the SLM 304L parts. With increasing VED, the overall relative density values increased. Accordingly, the highest density of 99 ± 0.5 % was attributed to the VED of 1400 J/mm^3. As discussed in Section 3.3, the formation of porosity due to gas entrapment, the presence of elongated voids due to lack of fusion, and the balling effect could result in lower relative densities at lower VEDs.

The overall trend of microhardness values was a slight increase at higher VEDs, as shown in Fig. 13(b). The highest microhardness value was 254 ± 7 HV, associated with VED of 280 J/mm^3. Relative density and microhardness values followed the same trend but with a different slope. This different slope could imply that the relative density values were strongly correlated to VEDs in contrast to microhardness values which were less strongly related to VEDs. Tucho *et al.* [18] reported a strong influence of relative density on the hardness values of SLM 316L in a limited range of 50–80 J/mm^3. Although in our study, the microhardness values decreased by decreasing VEDs, a significant correlation between relative density and microhardness values could not be found at VED of 117 − 1400 J/mm^3.

The engineering stress-strain curves of SLM 304L at VEDs of 700 and 175 J/mm^3 are plotted in Fig. 14. The corresponding relative density, YS, UTS, and elongation were listed in Table 7. Tensile data for wrought 304L SS (YS = 170 MPa and UTS = 485 MPa) was used for comparison [47]. At VED of 700 J/mm^3 and relative density of 99 ± 0.02 %, the YS and UTS values were measured to be 540 ± 15 MPa and 660 ± 20 MPa, respectively. At VED of 175 J/mm^3 and relative density of 97.5 ± 0.6 %, the YS and UTS values were measured to be 430 ± 12 MPa and 530 ± 24 MPa, respectively.

By comparing the tensile properties at two different relative densities of 97.5 % and 99 % it can be demonstrated that an increase of 1.5 % in density has a significant impact on tensile properties; improving YS from 430 ± 12 MPa to 540 ± 15 MPa (which is about 25 % improvement). Guan et al. [21] reported YS of 519 − 570 MPa and UTS of 651 − 717 MPa for fully dense 304 SS parts (~100 % density based on

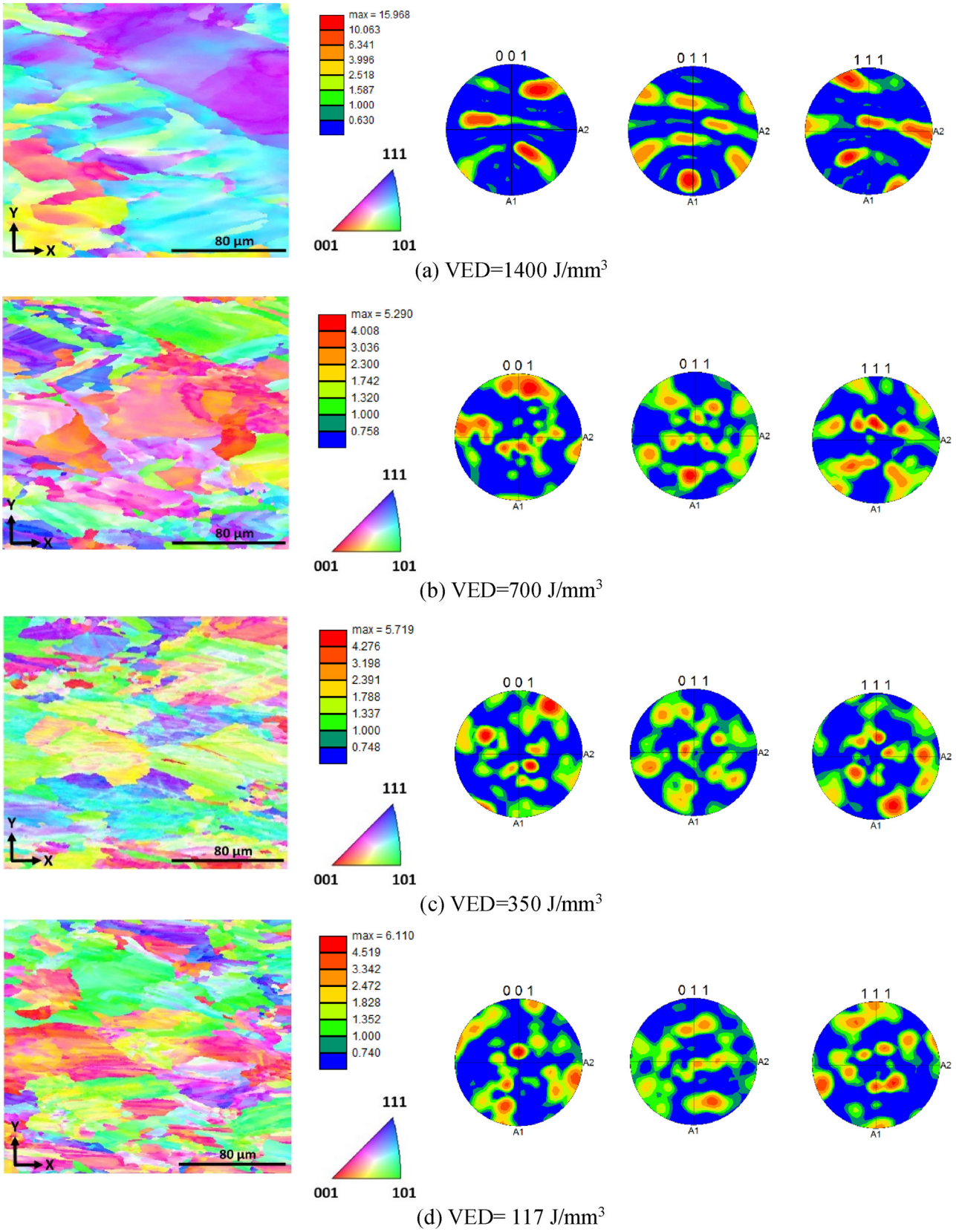

Fig. 12. Inverse pole figure and corresponding pole figures obtained from perpendicular to cross-section of samples SLM 304L at various VEDs of (a) 1400 J/mm^3, (b) 700 J/mm^3, (c) 350 J/mm^3 and (d) 117 J/mm^3.

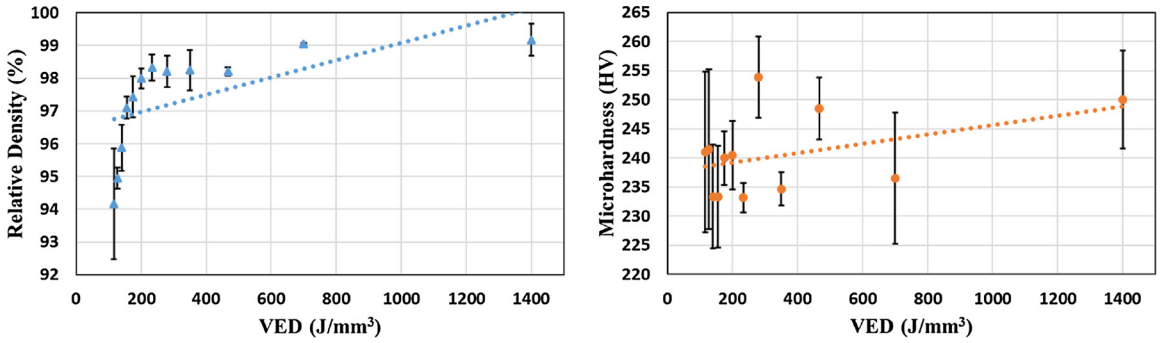

Fig. 13. (a) The relative density and (b) microhardness values of SLM 304L as a function of VEDs ranged from 117 − 1400 J/mm^3.

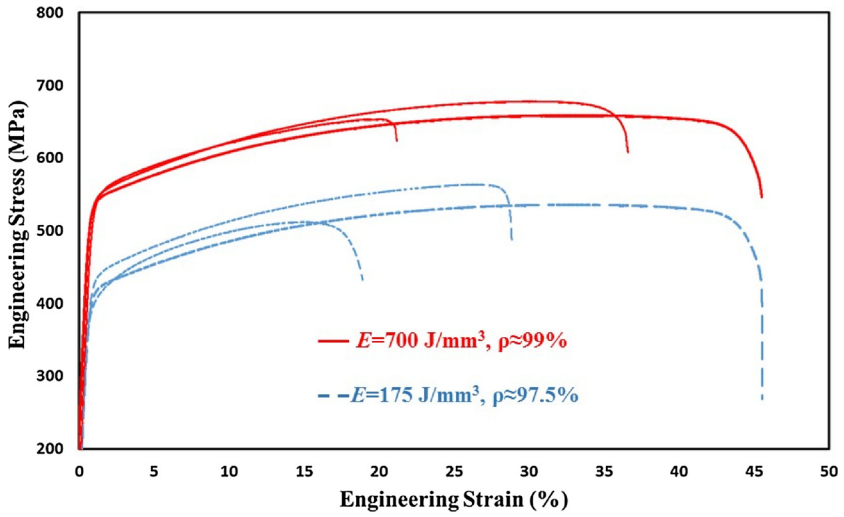

Fig. 14. Engineering stress-strain curve of 304L SLM at VED = 700 and 175 J/mm^3.

Table 7
Mechanical properties of SLM 304 at a relative density of 97.5 and 99 % (YS, UTS, and elongation of wrought 304L is reported).

Material	Yield Stress (MPa)	UTS (MPa)	Elongation (%)	VED (J/mm^3)
SLM 304, ρ = 99 ± 0.02 %,	540 ± 15	660 ± 20	36 ± 12	700
SLM 304, ρ = 97.5 ± 0.6 %,	430 ± 12	530 ± 24	32 ± 11	175
Wrought 304L [47]	170	485	40	N/A

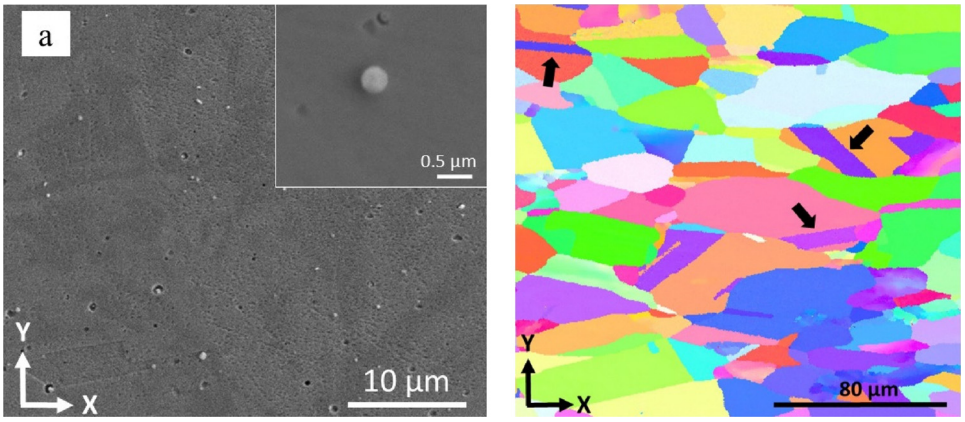

Fig. 15. (a) SEM micrograph of SLM (VED of 233 J/mm^3) and annealed 304L at T = 1200 °C for 2 h and (b) corresponding IPF map, showing annealing twins (arrows, pointing at annealing twins) and equiaxed grains.

their optical micrograph results) produced in a self-developed SLM machine. SLM process variables included layer thickness (20 − 40 μm), overlap rate (10–50 %) and hatch angle (90°-150°) [21]. The results in the current study showed the highest YS of 540 ± 15 MPa and UTS of 660 ± 20 MPa was achieved at a relative density of 99 ± 0.02 %, and were in agreement with the results reported by Guan's [21]. In another study by Elghany et al. [22] the YS of 182 MPa and UTS of 393 MPa were measured for SLM 304L with a relative density of 94 %.

Table 7 shows a high elongation of 30–40 % that can be attributed to the formation of twinning during the tensile test because it is a favorable deformation mechanism in 304L steel with low stacking fault. Deformation-induced twins were formed toward necking region in SLM 316L according to Pham et al. [48]. Twining spacing of 2 − 5 μm was measured by EBSD led to a good ductility of SLM 316L [48]. Nanotwins with a twinning spacing of 200 nm were identified in SLM 304, as shown in Fig. 10(b). In contrast to the formation of parallel twins in the deformed samples, nanotwins in Fig. 10(b) showed no preferred orientation. This is because of alternating scan strategies and scan speed that can change the direction of thermal stress and growth of twin boundaries.

The interaction of the twin boundary and dislocation increases the dislocation storage capacity resulting in higher tensile and creep properties. Twin boundaries act as grain boundaries and consequently enhance ductility [49,50]. Additionally, deformation twins with the spacing of tens to hundreds of nanometers show Hall-Petch behavior that can enhance mechanical properties [51]. Therefore, twining is a mechanism that can increase both strength and ductility simultaneously. The presence of nanotwins prior to tensile tests could generate more obstacles and potentially enhance the mechanical properties. The reported SFE for 304L SS is in the range of 8–40 $mJ.m^{-2}$ and for 316L is in the range of 14.2–78 $mJ\ m^{-2}$ [52]. Higher mechanical properties can be achieved in SLM 304L compared with SLM 316L due to the lower stacking fault energy of 304L and prior existence of nanotwins boundaries in SLM 304L.

3.7. Annealed SLM 304L

The sample with a VED of 233 J/mm^3 was annealed in vacuum at 1200 °C for 2 h. XRD result of the annealed sample is formerly shown in Fig. 3 and revealed only the austenitic phase. The retained δ-ferrite phase formed due to rapid cooling completely transformed to austenite during annealing.

After annealing microhardness value was reduced from 233 ± 3 HV to 208 ± 8 HV. As discussed in Section 3.6, the induced thermal stresses in SLM process led to the formation of nanotwins that could potentially act as a driving force of recrystallization [53]. Fig. 15(a) shows SEM micrograph of annealed SLM 304L. After annealing, the cellular substructure produced by the SLM process was disappeared, and no microsegregation was observed in cell wall indicating recrystallization of SLM 304L during annealing. Nanoparticles with a diameter of 20 − 80 nm, were coarsened to 200 − 500 nm due to diffusion in annealing as shown in the inset of Fig. 15(a).

Annealing twins are pointed out by arrows in the EBSD IPF map shown in Fig. 15(b). 304L SS is prone to the formation of annealing twins due to substantially lower stacking fault energy [53]. As a result, the grain morphology was transformed from columnar grains to more equiaxed grains with uniform grain size distribution as shown in Fig. 15(b).

4. Summary and conclusion

In this study, fully dense 304L SS parts were manufactured using SLM process. Effect of various VEDs on the microstructure, texture and mechanical properties are investigated after SLM and annealing. The primary findings from this study are as follows:

1 The absence of porosity and balling effect in the sample with VED of 1400 J/mm^3 (relative density of 99 ± 0.5 %) was attributed to the lower viscosity and a larger volume of melt. Furthermore, Marangoni convection facilitated the melt spread and filled the porosity more easily. The existence of a few small porosities could be due to gas entrapment during the process.
2 EBSD analysis illustrated a strong texture in the sample with a VED of 1400 J/mm^3 at the direction of [100], and a multicomponent texture on samples with VEDs of 750, 350 and 117 J/mm^3. This multicomponent texture was attributed to the higher rate of nucleation and porosity altering grains orientation from the easy growth direction of [100].
3 TEM analysis revealed the formation of thermally-induced nanotwins due to rapid cooling in the matrix of SLM 304L. Lower stacking fault energy of 304L (8 $mJ.m^{-2}$) could explain the presence of nanotwins. Furthermore, nanoparticles were observed with composition of Si, Mn, and O, likely due to lower enthalpy of formation of Si and Mn oxides, compared to the other elements within the 304L matrix.
4 Relative density and hardness values of SLM 304L were reduced by decreasing VEDs with different slopes. The highest relative density of 99 ± 0.5 % was associated with VED of 1400 J/mm^3, and the highest hardness of 254 ± 7 HV was obtained for VED of 280 J/mm^3. SLM 304L (ρ = 99 ± 0.02 %) exhibited considerably higher YS (540 ± 15 MPa) and UTS (660 ± 20 MPa) compared to the wrought 304L (170 MPa and 485 MPa, respectively).
5 After annealing a sample with VED of 233 J/mm^3 at T = 1200 °C, microhardness value was reduced to 208 ± 8 HV. The cellular substructure and elongated grains disappeared due to recrystallization. The nanoparticles were coarsened to 200 − 500 nm, which were substantially higher than the initial size of nanoparticles (20 − 80 nm).

Declaration of Competing Interest

All authors have participated in (a) conception and design, or analysis and interpretation of the data; (b) drafting the article or revising it critically for important intellectual content; and (c) approval of the final version.

This manuscript has not been submitted to, nor is under review at, another journal or other publishing venue.

The authors have no affiliation with any organization with a direct or indirect financial interest in the subject matter discussed in the manuscript.

Acknowledgments

The authors would like to acknowledge the funding of critical equipment provided by the Murdock Charitable Trust (Contract number: 2016231:MNL:5/18/2017), the Rapid Advancement of Process Intensification Deployment (RAPID) Institute and U.S. DOE for the financial support. The authors also thank the OSU electron microscopy center and ATAMI facility staff and director.

Appendix A. Supplementary data

Supplementary material related to this article can be found, in the online version, at doi:https://doi.org/10.1016/j.addma.2019.101011.

References

[1] B. Mueller, Additive manufacturing technologies–rapid prototyping to direct digital manufacturing, Assem. Autom. 32 (2) (2012).
[2] Y. Zhai, D.A. Lados, J.L. LaGoy, Additive manufacturing: making imagination the major limitation, Jom 66 (5) (2014) 808–816.
[3] B. Vayre, F. Vignat, F. Villeneuve, Metallic additive manufacturing: state-of-the-art review and prospects, Mech. Ind. 13 (2) (2012) 89–96.

[4] J. Strößner, M. Terock, U. Glatzel, Mechanical and microstructural investigation of nickel-based superalloy IN718 manufactured by selective laser melting (SLM), Adv. Eng. Mater. 17 (8) (2015) 1099–1105.
[5] S. Li, Q. Wei, Y. Shi, Z. Zhu, D. Zhang, Microstructure characteristics of Inconel 625 superalloy manufactured by selective laser melting, J. Mater. Sci. Technol. 31 (9) (2015) 946–952.
[6] H. Schwab, F. Palm, U. Kühn, J. Eckert, Microstructure and mechanical properties of the near-beta titanium alloy Ti-5553 processed by selective laser melting, Mater. Des. 105 (2016) 75–80.
[7] I. Yadroitsev, P. Krakhmalev, I. Yadroitsava, Selective laser melting of Ti6Al4V alloy for biomedical applications: temperature monitoring and microstructural evolution, J. Alloys Compd. 583 (2014) 404–409.
[8] E. Brandl, U. Heckenberger, V. Holzinger, D. Buchbinder, Additive manufactured AlSi10Mg samples using Selective Laser Melting (SLM): microstructure, high cycle fatigue, and fracture behavior, Mater. Des. 34 (2012) 159–169.
[9] S. Pasebani, M. Ghayoor, S. Badwe, H. Irrinki, S.V. Atre, Effects of atomizing media and post processing on mechanical properties of 17-4 PH stainless steel manufactured via selective laser melting, Addit. Manuf. 22 (2018) 127–137.
[10] L.E. Murr, E. Martinez, J. Hernandez, S. Collins, K.N. Amato, S.M. Gaytan, P.W. Shindo, Microstructures and properties of 17-4 PH stainless steel fabricated by selective laser melting, J. Mater. Res. Technol. 1 (3) (2012) 167–177.
[11] M. Ghayoor, S.B. Badwe, H. Irrinki, S.V. Atre, S. Pasebani, Water atomized 17-4 PH stainless steel powder as a cheaper alternative powder feedstock for selective laser melting, Materials Science Forum, Trans Tech Publ. 941, 2018, pp. 698–703.
[12] M. Averyanova, P. Bertrand, B. Verquin, Studying the influence of initial powder characteristics on the properties of final parts manufactured by the selective laser melting technology: a detailed study on the influence of the initial properties of various martensitic stainless steel powders on the final microstructures and mechanical properties of parts manufactured using an optimized SLM process is reported in this paper, Virtual Phys. Prototyp. 6 (4) (2011) 215–223.
[13] E. Liverani, S. Toschi, L. Ceschini, A. Fortunato, Effect of selective laser melting (SLM) process parameters on microstructure and mechanical properties of 316L austenitic stainless steel, J. Mater. Process. Technol. 249 (2017) 255–263.
[14] K. Saeidi, X. Gao, Y. Zhong, Z.J. Shen, Hardened austenite steel with columnar subgrain structure formed by laser melting, Mater. Sci. Eng. A 625 (2015) 221–229.
[15] R. Li, Y. Shi, Z. Wang, L. Wang, J. Liu, W. Jiang, Densification behavior of gas and water atomized 316L stainless steel powder during selective laser melting, Appl. Surf. Sci. 256 (13) (2010) 4350–4356.
[16] Z. Sun, X. Tan, S.B. Tor, W.Y. Yeong, Selective laser melting of stainless steel 316L with low porosity and high build rates, Mater. Des. 104 (2016) 197–204.
[17] T. Kurzynowski, K. Gruber, W. Stopyra, B. Kuźnicka, E. Chlebus, Correlation between process parameters, microstructure and properties of 316 L stainless steel processed by selective laser melting, Mater. Sci. Eng. A 718 (2018) 64–73.
[18] W.M. Tucho, V.H. Lysne, H. Austbø, A. Sjolyst-Kverneland, V. Hansen, Investigation of effects of process parameters on microstructure and hardness of SLM manufactured SS316L, J. Alloys Compd. 740 (2018) 910–925.
[19] P. Deng, Q. Peng, E.-H. Han, W. Ke, C. Sun, Z. Jiao, Effect of irradiation on corrosion of 304 nuclear grade stainless steel in simulated PWR primary water, Corros. Sci. 127 (2017) 91–100.
[20] S. Ziemniak, M. Hanson, Corrosion behavior of 304 stainless steel in high temperature, hydrogenated water, Corros. Sci. 44 (10) (2002) 2209–2230.
[21] K. Guan, Z. Wang, M. Gao, X. Li, X. Zeng, Effects of processing parameters on tensile properties of selective laser melted 304 stainless steel, Mater. Des. 50 (2013) 581–586.
[22] K. Abd-Elghany, D.L. Bourell, Property evaluation of 304L stainless steel fabricated by selective laser melting, Rapid Prototyp. J. 18 (5) (2012) 420–428.
[23] H. Yu, J. Yang, J. Yin, Z. Wang, X. Zeng, Comparison on mechanical anisotropies of selective laser melted Ti-6Al-4V alloy and 304 stainless steel, Mater. Sci. Eng. A 695 (2017) 92–100.
[24] Z. Wang, T.A. Palmer, A.M. Beese, Effect of processing parameters on microstructure and tensile properties of austenitic stainless steel 304L made by directed energy deposition additive manufacturing, Acta Mater. 110 (2016) 226–235.
[25] I. Yadroitsev, P. Krakhmalev, I. Yadroitsava, S. Johansson, I. Smurov, Energy input effect on morphology and microstructure of selective laser melting single track from metallic powder, J. Mater. Process. Technol. 213 (4) (2013) 606–613.
[26] D. Hann, J. Iammi, J. Folkes, A simple methodology for predicting laser-weld properties from material and laser parameters, J. Phys. D Appl. Phys. 44 (44) (2011) p. 445401.
[27] W.E. King, H.D. Barth, V.M. Castillo, G.F. Gallegos, J.W. Gibbs, D.E. Hahn, C. Kamath, A.M. Rubenchik, Observation of keyhole-mode laser melting in laser powder-bed fusion additive manufacturing, J. Mater. Process. Technol. 214 (12) (2014) 2915–2925.
[28] V. Gunenthiram, P. Peyre, M. Schneider, M. Dal, F. Coste, I. Koutiri, R. Fabbro, Experimental analysis of spatter generation and melt-pool behavior during the powder bed laser beam melting process, J. Mater. Process. Technol. 251 (2018) 376–386.
[29] U. Scipioni Bertoli, G. Guss, S. Wu, M.J. Matthews, J.M. Schoenung, In-situ characterization of laser-powder interaction and cooling rates through high-speed imaging of powder bed fusion additive manufacturing, Mater. Des. 135 (2017) 385–396.
[30] U.S. Bertoli, A.J. Wolfer, M.J. Matthews, J.-P.R. Delplanque, J.M. Schoenung, On the limitations of volumetric energy density as a design parameter for selective laser melting, Mater. Des. 113 (2017) 331–340.
[31] C. Yap, C. Chua, Z. Dong, An effective analytical model of selective laser melting, Virtual Phys. Prototyp. 11 (1) (2016) 21–26.
[32] R. Engeli, T. Etter, S. Hoevel, K. Wegener, Processability of different IN738LC powder batches by selective laser melting, J. Mater. Process. Technol. 229 (2016) 484–491.
[33] R.A. Young, The Rietveld Method Vol. 5 International union of crystallography, 1993.
[34] J. Elmer, S. Allen, T. Eagar, Microstructural development during solidification of stainless steel alloys, Metall. Trans. A 20 (10) (1989) 2117–2131.
[35] Y. Arata, F. Matsuda, S. Katayama, Solidification crack susceptibility in weld metals of fully austenitic stainless steels (Report I): fundamental investigation on solidification behavior of fully austenitic and duplex microstructures and effect of ferrite on microsegregation, Trans. JWRI 5 (2) (1976) 135–151.
[36] J.W. Fu, Y.S. Yang, J.J. Guo, W.H. Tong, Effect of cooling rate on solidification microstructures in AISI 304 stainless steel, Mater. Sci. Technol. 24 (8) (2013) 941–944.
[37] NASA, MSFC-SPEC-3717 Specification for Control and Qualification of Laser Powder Bed Fusion Metallurigical Processes, (2017).
[38] T. Iida, R.I. Guthrie, The Physical Properties of Liquid Metals, Clarendon Press, Walton Street, Oxford OX 2 6 DP, UK, 1988.
[39] A. Simchi, H. Pohl, Effects of laser sintering processing parameters on the microstructure and densification of iron powder, Mater. Sci. Eng. A 359 (1–2) (2003) 119–128.
[40] D. Wang, S. Wu, F. Fu, S. Mai, Y. Yang, Y. Liu, C. Song, Mechanisms and characteristics of spatter generation in SLM processing and its effect on the properties, Mater. Des. 117 (2017) 121–130.
[41] J.N. DuPont, Fundamentals of weld solidification, ASM Handbook Vol. 6A (2011).
[42] S. David, J. Vitek, Correlation between solidification parameters and weld microstructures, Int. Mater. Rev. 34 (1) (1989) 213–245.
[43] M. Ma, Z. Wang, X. Zeng, A comparison on metallurgical behaviors of 316L stainless steel by selective laser melting and laser cladding deposition, Mater. Sci. Eng. A 685 (2017) 265–273.
[44] Z. Sun, X. Tan, S.B. Tor, C.K. Chua, Simultaneously enhanced strength and ductility for 3D-printed stainless steel 316L by selective laser melting, NPG Asia Mater. 10 (4) (2018) 127–136.
[45] D.R. Gaskell, D.E. Laughlin, Introduction to the Thermodynamics of Materials, CRC Press, 2017.
[46] T. Niendorf, S. Leuders, A. Riemer, H.A. Richard, T. Tröster, D. Schwarze, Highly anisotropic steel processed by selective laser melting, Metall. Mater. Trans. B 44 (4) (2013) 794–796.
[47] A. Standard, Standard Specification for Chromium and Chromium-Nickel Stainless Steel Plate, Sheet, and Strip for Pressure Vessels and for General Applications, ASTM, West Conshohocken, PA, 2017.
[48] M.S. Pham, B. Dovgyy, P.A. Hooper, Twinning induced plasticity in austenitic stainless steel 316L made by additive manufacturing, Mater. Sci. Eng. A 704 (2017) 102–111.
[49] M. Merz, S. Dahlgren, Tensile strength and work hardening of ultrafine-grained high-purity copper, J. Appl. Phys. 46 (8) (1975) 3235–3237.
[50] G. Kaschner, C. Tomé, I. Beyerlein, S. Vogel, D. Brown, R. McCabe, Role of twinning in the hardening response of zirconium during temperature reloads, Acta Mater. 54 (11) (2006) 2887–2896.
[51] L. Lu, R. Schwaiger, Z. Shan, M. Dao, K. Lu, S. Suresh, Nano-sized twins induce high rate sensitivity of flow stress in pure copper, Acta Mater. 53 (7) (2005) 2169–2179.
[52] G.M. de Bellefon, J. van Duysen, K. Sridharan, Composition-dependence of stacking fault energy in austenitic stainless steels through linear regression with random intercepts, J. Nucl. Mater. 492 (2017) 227–230.
[53] Y. Jin, M. Bernacki, G.S. Rohrer, A.D. Rollett, B. Lin, N. Bozzolo, Formation of annealing twins during recrystallization and grain growth in 304L austenitic stainless steel, Materials Science Forum, Trans Tech Publ. 753, 2013, pp. 113–116.